Orbital phasing of the Paleocene-Eocene Thermal Maximum

Victor A. Piedrahita[a*], Simone Galeotti[b,c], Xiang Zhao[a], Andrew P. Roberts[a], Eelco J. Rohling[a,d], David Heslop[a], Fabio Florindo[c,e], Katharine M. Grant[a], Laura Rodríguez-Sanz[a], Daniele Reghellin[b], Richard E. Zeebe[f]

[a]Research School of Earth Sciences, Australian National University, ACT 2601, Canberra, Australia

[b]Dipartimento di Scienze Pure e Applicate, Università degli Studi di Urbino, 61029, Urbino, Italy

[c]Institute for Climate Change Solutions, Via Sorchio 61040, Frontone, Pesaro e Urbino, Italy

[d]School of Ocean and Earth Science, University of Southampton, National Oceanography Centre, SO14 3ZH, Southampton, UK

[e]Istituto Nazionale di Geofisica e Vulcanologia, Via di Vigna Murata 605, 00143, Rome, Italy

[f]School of Ocean and Earth Science and Technology, Department of Oceanography, University of Hawaii, 1000 Pope Road, Honolulu, HI 96822, USA

***Corresponding author**: victor.piedrahitavelez@anu.edu.au

Highlights

- Orbital controls influenced Paleocene-Eocene Thermal Maximum triggering.
- The Paleocene-Eocene Thermal Maximum appeared close to a long eccentricity maximum.

- The Paleocene-Eocene Thermal Maximum appeared close to a short eccentricity maximum.
- The Paleocene-Eocene Thermal Maximum contained multiple lysocline shoaling events.

Abstract

Paleocene-Eocene sedimentary archives record a series of global warming events called hyperthermals. These events occurred across a long-term increasing temperature trend and were associated with light carbon injections that produced carbon isotope excursions (CIEs). Early Eocene hyperthermals occurred close to both long (~405 kyr) and short (~100 kyr) eccentricity maxima. It has been proposed that under long-term global warming, orbital forcing of climate crossed a thermodynamic threshold that destabilized carbon reservoirs and produced Early Eocene hyperthermals. However, orbital control on triggering of the largest hyperthermal, the Paleocene-Eocene Thermal Maximum (PETM), remains unclear. Identification of the precise orbital phasing of the PETM has been hindered by extensive calcium carbonate ($CaCO_3$) dissolution, which introduces uncertainty into PETM age models. Here, we report orbital signatures in marine sediments from Contessa Road (Italy), a western Tethyan section with reduced PETM $CaCO_3$ dissolution compared to other deep ocean sites. Orbitally controlled lysocline depth adjustments and orbital phasing of the PETM CIE onset close to both long and short eccentricity maxima are documented here. Precession-based age models from the well-resolved PETM section of Ocean Drilling Program (ODP) Site 1262 (South Atlantic) confirm these results and reveal that the PETM CIE onset was partially triggered by an orbitally controlled mechanism. Climate processes associated with orbital forcing of both long and short eccentricity maxima played an important role in triggering the carbon cycle perturbations of all Paleocene-Eocene CIE events.

Keywords: Paleocene-Eocene Thermal Maximum (PETM), orbital control, $CaCO_3$ dissolution, long eccentricity maximum, short eccentricity maximum.

1. Introduction

Late Paleocene-early Eocene climate records (~58-52 Ma) contain evidence of a series of light carbon injections that produced negative carbon isotope excursions (CIEs) (Cramer et al., 2003; Zachos et al., 2010; Westerhold et al., 2020). Some of these short-lived (<200 kyr) carbon cycle perturbations were associated with global warming events called hyperthermals (Cramer et al., 2003; Zachos et al., 2010). The Paleocene-Eocene Thermal Maximum (PETM, ~56 Ma) was the largest hyperthermal, and was followed by early Eocene hyperthermals–i.e., the Eocene Thermal Maximum (ETM) 2 (~54 Ma) and ETM 3 (~53 Ma)– and smaller carbon cycle perturbations–i.e., the H2, I1 and I2 events (Lourens et al., 2005; Westerhold et al., 2007; Zachos et al., 2010; Zeebe and Lourens, 2019). All of these events occurred across a long-term increasing temperature trend (Westerhold et al., 2020). Under gradual long-term warming and orbital forcing of long (~405 kyr) and short (~100 kyr) eccentricity maxima, climate is thought to have crossed a thermodynamic threshold that destabilized carbon reservoirs and triggered light carbon releases to the climate system (Fig. 1a; Lunt et al., 2011; DeConto et al., 2012; Kirtland Turner et al., 2014). This driving mechanism explains the origins of early Eocene hyperthermals, all of which appeared close to long eccentricity maxima (Galeotti et al., 2010; Zachos et al., 2010; Kirtland Turner et al., 2014; Laurin et al., 2016). However, the influence of this orbitally controlled mechanism on PETM CIE triggering remains unclear.

The PETM had a ~170-220 kyr duration that has been related to at least two light carbon injections (Röhl et al., 2000, 2007; Murphy et al., 2010; Westerhold et al., 2018; Zeebe and Lourens, 2019; van der Meulen et al., 2020). The initial PETM light carbon injection has been partially interpreted to have resulted from thermogenic methane releases associated with North Atlantic Igneous Province activity (Svensen et al., 2004; Sluijs et al., 2007; Kender et al., 2021). Volcanic activity has been suggested to have promoted widespread warming before the PETM, which may have subsequently destabilized carbon reservoirs and triggered the PETM CIE (Sluijs et al., 2007; Frieling et al., 2019; Kender et al., 2021). However, North Atlantic Igneous Province activity was reduced at the PETM CIE onset (Kender et al., 2021), which suggests that additional positive carbon cycle feedbacks, likely related to other mechanisms–i.e., orbitally controlled processes (Lourens et al., 2005; Lunt et al., 2011; DeConto et al., 2012; Zeebe and Lourens, 2019)–may have also played a role in PETM CIE triggering.

Carbon releases following the PETM CIE onset produced a long (>100 kyr) lysocline shoaling event with extensive calcium carbonate ($CaCO_3$) dissolution (Fig. 1b; Zeebe et al., 2009; Zeebe, 2013; Bowen, 2013; Frieling et al., 2016; Lyons et al., 2019). This prolonged $CaCO_3$ dissolution interval has not been identified in succeeding early Eocene CIEs. Some early Eocene carbon cycle perturbations were paired events associated with two different carbon injections. These carbon releases caused $CaCO_3$ dissolution layers that coincided with consecutive maxima of short eccentricity cycles—i.e., the ETM 2 and H2, and I1 and I2 events (Cramer et al., 2003; Zachos et al., 2010; Laurin et al., 2016; Westerhold et al., 2018). Extensive PETM $CaCO_3$ dissolution produced poor recording of orbitally controlled $CaCO_3$ dissolution cycles in marine sediments, which has affected the accuracy of Paleocene-Eocene astrochronological age models and hindered assessments of orbital controls on PETM CIE triggering.

The PETM $CaCO_3$ dissolution interval duration has been debated due to limitations of astrochronological age models and temporal differences of lysocline depth variations at diverse locations (Zeebe et al., 2009). Age model calibrations have been carried out to estimate the PETM $CaCO_3$ dissolution interval duration at the well-resolved PETM section from the South Atlantic Ocean Drilling Program (ODP) Site 1262 (Fig. 1c; ~3600 m paleowater depth). A ~120 kyr duration for the PETM $CaCO_3$ dissolution interval at ODP Site 1262 was estimated using precession-based age models and age calibrations between terrestrial and marine records (Zachos et al., 2005; Aziz et al., 2008; Westerhold et al., 2018; van der Meulen et al., 2020). Alternatively, orbital tuning of ODP Site 1262 records to the recent ZB18a astronomical solution (Zeebe and Lourens, 2019) indicates a 170 ± 30 kyr duration for the same time interval, despite uncertain astronomical solutions beyond ~50 Ma (e.g., Laskar et al., 2004; Zeebe and Lourens, 2019). These Paleocene-Eocene chronologies reveal a period of $CaCO_3$-rich sedimentation, enhanced $CaCO_3$ burial, and carbon sequestration following the PETM $CaCO_3$ dissolution interval (Kelly et al., 2010; Luo et al., 2016; Penman et al., 2016). However, differences among Paleocene-Eocene age models hinder identification of orbital phasing in relation to the PETM CIE onset. The PETM CIE onset has been suggested to lie close to a long eccentricity maximum (Lourens et al., 2005; Galeotti et al., 2010; Zeebe and Lourens, 2019) or with a quarter of a period offset after a long eccentricity maximum (Westerhold et al., 2007). These contrasting interpretations do not allow clear recognition of the possible influence of an orbitally controlled driving mechanism on PETM CIE triggering.

Marine sedimentary sections with reduced PETM $CaCO_3$ dissolution may preserve better orbital signals across the PETM $CaCO_3$ dissolution interval, which might enable more accurate estimation of the duration of this interval. Orbital signals from these locations are accompanied by amplitude modulation (AM) and frequency modulation (FM) patterns (*see Materials and methods*) that can refine Paleocene-Eocene chronologies and reveal orbital phasing of the PETM CIE onset. Modeling experiments suggest that Tethys Ocean sediments experienced less extensive PETM $CaCO_3$ dissolution compared to other locations (Zeebe et al., 2009). These results are confirmed by PETM records from the western Tethyan Contessa Road section, Italy (Fig. 1c-d; ~1000-1500 m paleowater depth). Two marly horizons separated by a limestone layer cover the PETM $CaCO_3$ dissolution interval at Contessa Road (Fig. 2a-b; Galeotti et al., 2000; Giusberti et al., 2009; Galeotti et al., 2010). The lowest $CaCO_3$ contents across the first and second Contessa Road marly horizons are ~35% and ~65%, respectively (Fig. 2c; Giusberti et al., 2009), which contrast with $CaCO_3$ values from other marine sections that are close to 0%–i.e., ODP Site 1262 (Fig. 1b; Zachos et al., 2005). Here, we use the exceptionally well-preserved PETM records from Contessa Road to constrain the PETM $CaCO_3$ dissolution interval duration at this section. We assess AM and FM patterns in orbital signals from Contessa Road to identify orbital phasing of the PETM CIE onset. We also generate a probabilistic estimate of orbital phasing of the PETM CIE onset using a new refined chronology for ODP Site 1262, which provides a broader perspective on the orbital configuration in which the PETM CIE onset occurred.

2. Materials and methods

2.1 Amplitude and frequency modulation

Astrochronological age models, and associated AM and FM patterns of precession and short eccentricity can help to reveal orbital phasing of the PETM. These approaches are independent of uncertain astronomical solutions beyond ~50 Ma (Laskar et al., 2004; Zeebe and Lourens, 2019). Orbital precession (~21 kyr) and short eccentricity are tied to short and long eccentricity phases, respectively (Berger and Loutre, 1991). Hence, AM of precession and short eccentricity indicate cyclicity in their signal modulators (Laurin et al., 2005, 2016, 2021; Meyers et al., 2015). These modulations include orbital components of 19 and 23 kyr for precession, and 95 and 124 kyr for short eccentricity (Laskar et al., 2004). Systematic shifts in frequencies of orbital components are described as FM patterns (Laurin et al., 2016, 2021). FM defines positive and negative interference of orbital frequencies in wavelength components of evolutive harmonic analysis (EHA) (Rial, 1999; Meyers et al., 2001; Laurin et al., 2016). Negative interference of FM is associated with bifurcations of wavelength components, which indicates minimal conditions of the modulator—i.e., bifurcations of precession components (known as P1 and P2) reveal short eccentricity minima, and bifurcations of short eccentricity components (known as E2 and E3) indicate long eccentricity minima (Laurin et al., 2016). In contrast, positive interference of FM, which is identified by junctions of wavelength components, suggests modulator maxima—i.e., junctions of precession components reveal short eccentricity maxima and junctions of short eccentricity components indicate long eccentricity maxima (Laurin et al., 2016).

2.2 Contessa Road

The Contessa Road section (lat. 43°22’47’’N; long. 12°33’50’’E) exposes Paleocene-Eocene rocks of the Scaglia Rossa Formation (Galeotti et al., 2000, 2010). This sedimentary unit consists of reddish limestones and marls that were deposited in the western Tethyan Umbria-Marche Basin (Giusberti et al., 2009). Contessa Road sedimentation mainly consisted of pelagic $CaCO_3$ deposition with minimal detrital mineral inputs from northern Africa and southwestern Europe (Fig. 1d; Coccioni et al., 2019). The detrital fraction of Contessa Road carbonates includes quartz, hematite, barite, magnetite, and clay minerals (Giusberti et al., 2009; Galeotti et al., 2010; Coccioni et al., 2019). However, some studies have hypothesized that magnetite and barite are biomineralization products (Giusberti et al., 2009; Coccioni et al., 2019).

Contessa Road has well-developed magnetostratigraphic and biostratigraphic age constraints that allowed identification of the Cretaceous/Paleogene boundary. This major geological event has been assigned as 0 m depth at Contessa Road (e.g., Galeotti et al., 2000, 2010), and was followed by an extensive record of Paleocene-Eocene carbon cycle perturbations that mainly appeared between Chron 25n and 24n.1n, and between calcareous nannofossil zones NP8/NP9 and NP11 (Fig. 2a; Galeotti et al., 2010; Coccioni et al., 2019). These age constraints correspond to the 26-46 m depth interval at Contessa Road, which contains multiple $CaCO_3$ dissolution horizons that have been associated with Paleocene-Eocene carbon cycle perturbations (Fig. 2a; Galeotti et al., 2000, 2010). The $CaCO_3$ dissolution layers have also been used to generate early Eocene cyclostratigraphic frameworks that are interpreted to indicate orbital control on $CaCO_3$ dissolution cycles (Galeotti et al., 2010). Orbital control of $CaCO_3$ sedimentation has been identified from inverse relationships between $CaCO_3$ and terrigenous input indicators–i.e., magnetic susceptibility (Galeotti et al., 2010; Francescone et al., 2018); however, orbital controls have not been assessed for the Contessa Road PETM record. Contessa Road presents anti-correlation of quartz and $CaCO_3$ records, which is interpreted to indicate that siliciclastic sedimentation depended exclusively on continental detrital inputs (Giusberti et al., 2009) with no important biogenic Si contribution.

Paleocene-Eocene carbon cycle perturbations recorded in the Scaglia Rossa Formation appear in different outcrops across Contessa Road. The outcrop that contains the ~30-33 m interval of this section has two marly horizons separated by a limestone layer within magnetochron

C24r and calcareous nannofossil biozone NP10, which allowed recognition of the PETM $CaCO_3$ dissolution interval at Contessa Road (Fig. 2a-c; Galeotti et al., 2000, 2010). Previous and succeeding CIE events are identified in other outcrops (e.g., Galeotti et al., 2010). PETM marly layers at Contessa Road resulted from lysocline shoaling events that brought about different faunal changes (Giusberti et al., 2009). These lysocline shoaling events were separated by a lysocline deepening period that is indicated by limestones (Fig. 2b; Galeotti et al., 2000; Giusberti et al., 2009). The first marly horizon coincides with the PETM CIE onset ~31.26 m above the Cretaceous/Paleogene boundary. The PETM CIE onset is followed by low stable carbon isotope ($\delta^{13}C$) values that started increasing during the second PETM marly layer (Fig. 2d; Giusberti et al., 2009).

2.3 X-ray fluorescence measurements

For this study, we sampled the PETM outcrop at Contessa Road (30-33 m interval) continuously at 1-cm resolution for X-ray fluorescence (XRF) analyses. Samples were cut to expose flat surfaces for measurements. These were made using a third generation Avaatech XRF Core Scanner at 10 kV (current = 0.5 mA, count time = 60 s, and no filter) with a 16 mm^2 sample area. XRF data were acquired using a Canberra X-PIPS silicon drift detector. Samples were cleaned before measurement and were fixed over plastic holders for discrete measurement of each sample. Sample spacing in the core scan table was 20 cm to avoid interference between measurements. Contessa Road carbonate samples are lithified and do not release dust when in contact with the detector. Analyses of raw X-ray spectra were made by iterative least squares analysis in the Win Axil software from Canberra Eurisys. Standards were run multiple times between measurement sets to test measurement reliability, and to identify possible detector contamination. 105 replicate measurements were carried out for probabilistic uncertainty assessment. Standard deviation (1σ) of these measurements correspond to 2.7%, 1.6%, and 3.0% for Fe, Ca, and Si, respectively. All experiments were performed at the Australian National University.

2.4 Probabilistic uncertainty assessments and spectral analysis of Contessa Road records

Probabilistic uncertainty assessments for Contessa Road Fe, Ca, and Si records were used to develop astrochronological age models using Monte Carlo simulations. Initially, logarithmic transformation was applied to Fe and Si records to minimize the effects of large variability between the marly interval and pre-marly and post-marly intervals. Logarithmic transformation has also been applied to different Paleocene-Eocene XRF records from pelagic carbonate sections (e.g., Westerhold et al., 2007), which indicates that logarithmic transformation allows clear recognition of orbitally controlled $CaCO_3$ dissolution cycles. Then, Fe, Ca, and Si records were assigned standard deviations (1σ). A standard deviation (1σ) was assigned for depth as half the spacing between successive samples ($1\sigma = 0.5$ cm for XRF data), and standard deviations (1σ) for XRF data were estimated for each element using replicate measurements. Individual data points were sampled randomly within their uncertainties. 10,000 Monte Carlo simulations were produced to generate empirical distributions from which the mean and standard error (SE) were estimated at each depth. To avoid depth reversals, the stratigraphic order of samples was reviewed after Monte Carlo simulations. Mean and SE were then interpolated to fixed depth points.

To carry out spectral analysis of Contessa Road records, Fe, Ca, and Si records were detrended with a locally estimated scatterplot smoothing (LOESS) filter that uses 35% of the entire record length for each local regression window. Data variability indicates that detrending should be carried out via subtraction of non-parametric, rather than parametric, trends (*see Results*; Fig 2e-g). Power spectra were generated using the Fast Fourier transform

(FFT) and discrete Fourier transform (DFT) routines of the Power Spectrum VI function of LabView 2019. The power spectrum S_{xx} (*f*) of a function *x*(*t*) is indicated by:

$$S_{xx}(f) = X(f)X(f)^{*} = |X(f)|^{2},$$

where $X(f)$ is the Fourier transform (F) product of *x*(*t*), and $X(f)^{*}$ indicates the complex conjugate of $X(f)$. The Power Spectrum VI function of LabView 2019 produces similar power spectra to those obtained using the periodogram and multi-taper methods in the Acycle software (Li et al., 2019), which validates our approach (*see Supplemental information*). Spectral analyses of detrended records were made for each Monte Carlo iteration, which enables generation of empirical distributions from which the mean and SE were estimated. Data were then reviewed to avoid reversals and interpolated to fixed frequencies which allowed production of probabilistic-based power spectra for Contessa Road XRF records.

First-order order autoregressive (AR1) processes were fitted to the background mean power spectrum using a Monte Carlo approach (Li et al., 2019; Husson, 2022). This method allowed estimation of 90% and 95% confidence levels from the AR1 fits. The power spectrum of the AR1 process for a frequency f is indicated by:

$$S(f) = S_0 \frac{1-\rho_1^2}{1-2\rho_1 \cos\pi(\frac{f}{f_N})+\rho_1^2},$$

where f_N is the Nyquist frequency and the average value of a power spectrum related to the white-noise variance (S_0) is given by:

$$S_0 = \frac{\sigma^2}{1-\rho_1^2},$$

where ρ_1 corresponds to the lag-one autocorrelation coefficient, and σ^2 is the variance of a white-noise sequence ε (Mann and Less, 1996).

Frequency components associated with orbital signals from probabilistic-based power spectra were isolated using Gaussian bandpass filters also using LabView 2019. Each Monte Carlo iteration from detrended records was filtered, which allowed generation of empirical distributions from which the mean and SE were estimated. The stratigraphic order of samples was reviewed after Monte Carlo simulations to avoid depth reversals and data were then interpolated to fixed depth points. This process allowed isolation of probabilistic-based filtered orbital signals such as mean short eccentricity and mean precession with their respective uncertainty envelopes (2SE).

EHA (Meyers et al., 2001; Laurin et al., 2016, 2021) was carried out using the Fast Fourier Transform LAH (FFT LAH) method within the Acycle software (Li et al., 2019). Sliding windows that move in consecutive steps are used for EHA estimation. Details of the values used for sliding windows and steps in each analysis are given in the respective figure captions.

2.5 Contessa Road age models and AM patterns

Filtered mean precession and short eccentricity signals were used to identify AM patterns using the Amplitude Modulation tool of the Acycle software (Li et al., 2019). Filtered mean precession signals of the different XRF records were also used to produce astrochronological age models. Each precession cycle was assigned a 21 kyr period to produce a different chronology for each Contessa Road XRF record. Filtered precession signals from Contessa Road contain uncertainty envelopes that result from the error propagation. However, only the filtered mean precession signals were used for Contessa Road age model development. All datasets from Contessa Road were transferred into the time domain and were then set to 0 at the PETM CIE onset. Contessa Road records were then interpolated every 2.5 kyr, which corresponds to the average age spacing between samples, to produce age-domain EHA.

3. Results

3.1 Orbital signatures of the Contessa Road records

PETM marly layers, and thinner horizons with partial $CaCO_3$ dissolution, coincide with Fe and Si concentration increases and Ca reductions at Contessa Road (Fig. 2e-g). Depth-domain EHA of XRF records reveal a dominant wavelength component that has a frequency range of ~2 cycles m^{-1} across pre-PETM and post-PETM limestones, and a frequency range of ~3.5 cycles m^{-1} across the PETM marly horizons (dashed white lines; Fig. 2c-f). This wavelength component variation suggests sedimentation rate changes across Contessa Road (*see below*); therefore, to avoid impacts from sedimentation rate variations on the time-series, we divided the Contessa Road record into pre-marly (30.00-31.25), marly (31.20-31.75 m), and post-marly (31.70-33.00 m) intervals (Fig. 2b-g) and performed spectral analysis on each segment.

Power spectra of Fe, Ca, and Si records contain spectral peaks with means that exceed the 95% confidence level (Fig. 3). This indicates that on average Monte Carlo iterations of these time series contain statistically significant components (Mann and Lees, 1996). Magnetochron C24r had a ~3.2 Myr duration and is recorded over a ~12.6-m interval at the Contessa Road section (Galeotti et al., 2010; Francescone et al., 2018). Therefore, an average sedimentation rate of ~0.4 cm kyr^{-1} for C24r at Contessa Road can be estimated. Spectral analysis of the whole Contessa Road section indicates spectral peaks with ~0.36 m, ~0.09 m, and ~0.07 m periods. These peaks correspond to, based on the average sedimentation rate, ~90 kyr, ~22 kyr, and ~17 kyr periods, respectively (Fig. 3a), and can be associated with short eccentricity and precession. Other spectral peaks with frequencies between ~5 and 10 cycles m^{-1} exceed the 95% confidence level in power spectra for the entire Contessa Road section; however, these spectral peaks are not regularly identified in power spectra for the respective Contessa Road pre-marly, marly, and post-marly intervals. Hence, signals associated with these peaks are not discussed further.

The pre-marly and post-marly intervals have similar compositional characteristics, and wavelength component frequencies (Fig. 2b-g). Therefore, spectral peak periods for these intervals were estimated using an average ~0.4 cm kyr^{-1} sedimentation rate. Considering this average sedimentation rate, our 1-cm sampling resolution corresponds to an average sample spacing of ~2.5 kyr, which indicates a ~300 kyr duration for each interval. Spectral peaks with ~0.42 m and ~0.43 m periods for the pre-marly and post-marly intervals, respectively, can be attributed to short eccentricity due to their ~100-kyr periods (Fig. 3b, d). We note, however, that short eccentricity in the post-marly interval is weak in the Ca and Si records and do not reach the 95% confidence level (Fig. 3d). Spectral peaks with ~0.09 m periods in the pre-marly and post-marly intervals can be related to precession because of their ~22 kyr periods (Fig. 3b, d). The marly interval has spectral peaks with ~0.29 m and ~0.06 periods (Fig. 3c). Periodicity variations of the dominant spectral peaks of the marly, pre-marly and post-marly intervals (a spectral peak with a ~0.29 m period *versus* spectral peaks with ~0.42-0.43 m periods) suggest a sedimentation rate drop. The ~1.5 cycles m^{-1} difference of the dominant wavelength component between PETM marly horizons and pre-PETM and post-PETM limestones (Fig. 2e-g) confirms this assumption. These frequency changes in spectral peaks and wavelength components allow estimation of a sedimentation rate drop due to PETM $CaCO_3$ dissolution from ~0.4 cm kyr^{-1} to ~0.3 cm kyr^{-1} across the marly interval. This estimate indicates a ~3.3 kyr sample spacing across the marly interval, which reveals a ~180 kyr duration for this interval. Considering the reduced sedimentation rate, spectral peaks in the marly interval indicate cycles with ~94 kyr and ~23 kyr periods that can be related to short eccentricity and precession, respectively (Fig. 3b-d).

Gaussian bandpass filters with bandwidths of 2.38 ± 1.20 (1σ) cycles m^{-1} (~70-210 kyr), 3.56 ± 1.20 cycles m^{-1} (~70-141 kyr), and 2.29 ± 1.20 cycles m^{-1} (~70-230 kyr) for the pre-marly, marly, and post-marly intervals, respectively, were used to isolate short eccentricity signals. Short eccentricity signals were isolated for the Ca and Si records for the post-marly interval despite their poorly developed short eccentricity signal. Comparisons of probabilistic power spectra to periodograms of these records (see *Supplementary information*) indicate that the Si record contains a statistically significant peak that can be associated with short eccentricity in the post-marly interval. The Ca record in the post-marly interval periodogram also contains a week short eccentricity signal (see *Supplementary information*); however, the well-identified anti-correlation between Fe and Ca indicated by probabilistic uncertainty assessments (Fig. 2e-f) and filtered short eccentricity signals (Fig. 4a-b) reveal that the Contessa Road Ca record may also contain short eccentricity signals in the post-marly interval. Nevertheless, our interpretations of Ca in the post-marly interval do not depend exclusively on this record because we also compare the filtered short eccentricity signal of Fe and Si. Precession signals were extracted using Gaussian bandpass filters with bandwidths of 11.10 ± 3.70 cycles m^{-1} (~17-34 kyr), 14.25 ± 5.00 cycles m^{-1} (~17-36 kyr), and 11.45 ± 3.50 cycles m^{-1} (~17-31 kyr) for the pre-marly, marly, and post-marly intervals, respectively. Application of such wide Gaussian bandpass filters was based on short eccentricity and precession periodicities and ensures that all short eccentricity and precession components were captured. Isolated orbital signals have good visual correlation with detrended records (Fig. 4, 5a, c, e), which validates the consistency of the Gaussian bandpass filter bandwidths.

4. Discussion

3.1 Duration of the PETM $CaCO_3$ dissolution interval at Contessa Road

The inverse relationship between filtered orbital signals from Ca and detrital elements reflects previously identified orbitally controlled $CaCO_3$ dissolution cycles at Contessa Road (Fig. 5; Galeotti et al., 2010). The PETM CIE onset at this section coincided with a lysocline shoaling event that caused partial $CaCO_3$ dissolution over a ~42 kyr duration (precession cycles 0 and 1 in Fig. 5a, c, e). This event was followed by a lysocline deepening period that reestablished pre-PETM $CaCO_3$-rich sedimentation (Fig. 5c; Giusberti et al., 2009). Fe and Si records indicate that the PETM lysocline deepening at Contessa Road lasted nearly three precession cycles (precession cycles 2, 3, and 4 in Fig. 5a, e). Alternatively, orbital signals extracted from the Ca record reveal poor development of precession cycle 3, which suggests that only two precession cycles covered this interval (precession cycles 2 and 4 in Fig. 5c). This lysocline deepening period at Contessa Road was punctuated by a second, less extensive, lysocline shoaling event (Giusberti et al., 2009) that spanned one and a half precession cycles (precession cycles 5 and 6 in Fig. 5a, c, e). After this second partial $CaCO_3$ dissolution interval, pre-PETM $CaCO_3$-rich sedimentation was reestablished, and extensive PETM $CaCO_3$ dissolution ended. Considering differences between filtered precession signals at Contessa Road, we estimate that the PETM $CaCO_3$ dissolution interval lasted ~5.5-6.5 precession cycles at this section.

3.2 Was the PETM close to a short eccentricity maximum?

Orbital signals within Contessa Road pelagic carbonates allow clear recognition of AM and FM patterns. AM of precession (purple dashed lines in Fig. 5a, c, d) correlates relatively well with filtered short eccentricity signals. However, this relationship is less clear between precession cycles 8 and 12 (Fig. 5a, c, e). Considering a ~116-137 kyr PETM $CaCO_3$

dissolution interval duration, and a total PETM duration of ~170-220 kyr (Röhl et al., 2007; Murphy et al., 2010; Westerhold et al., 2018; Zeebe and Lourens, 2019; van der Meulen et al., 2020), cycles 8 to 12 coincide with a carbon sequestration period with enhanced $CaCO_3$ burial. This interval records accelerated $CaCO_3$-rich sedimentation that may have been related partially to either accelerated chemical weathering (Kelly et al., 2010; Penman et al., 2016) and/or biological carbonate compensation (Luo et al., 2016), which are non-orbitally controlled processes that may have slightly disturbed AM patterns. Alternatively, FM patterns obtained from filtered precession signals reveal two precession components (P1 and P2; Fig. 5) that indicate negative interference patterns associated with short eccentricity minima between precession cycles 7 and 9, and between precession cycles 13 and 14 (Fig. 5). These patterns correlate well with filtered short eccentricity signals, which clarifies the orbital configuration across this interval of enhanced $CaCO_3$ burial and carbon sequestration.

FM patterns allow recognition of the orbital phasing of PETM marly horizons at Contessa Road. Junctions of the P1 and P2 components reveal that these layers appeared close to short eccentricity maxima (Fig. 5b, d, f). Well-developed AM of precession and filtered short eccentricity signals confirm this observation, and indicate that the PETM marly horizons occurred in ascending flanks of short eccentricity cycles, close to short eccentricity maxima (Fig. 5a, c, e). The $CaCO_3$-rich sedimentation interval that separates the PETM marly horizons at Contessa Road coincided with a short eccentricity minimum, which is identified by negative interference of P1 and P2 components, AM of precession, and filtered short eccentricity signals (Fig. 5). These patterns reveal orbital controls on lysocline depth variations, which promoted development of the same sedimentation patterns as other early Eocene CIE events at Contessa Road–i.e., the ETM 2 and H2 events (Galeotti et al., 2010). This evidence also suggests that the PETM marly horizons at Contessa Road had a similar orbital phasing as other early Eocene hyperthermals in terms of short eccentricity (Zachos et al., 2010).

Identification of orbital phasing of the PETM with respect to short eccentricity has been also assessed at ODP Site 1262 (Westerhold et al., 2007; Zachos et al., 2010). Orbital signals from ODP Site 1262 redness over greenness (a*) and Fe records have increased values preceding the PETM, which has been used to suggest that the PETM CIE onset likely coincided with a short eccentricity maximum (Zachos et al., 2010). Orbitally controlled lysocline depth variations recorded by Contessa Road pelagic carbonates allow recognition of the orbital phasing of the PETM CIE onset with respect to short eccentricity. This event, according to AM of precession patterns, preceded a short eccentricity maximum by half a precession cycle (Fig. 5a, c, e). Alternatively, if only filtered short eccentricity signals are considered, the PETM CIE occurred one precession cycle before a short eccentricity maximum (Fig. 5a, c, e). This evidence suggests that the PETM CIE onset may have appeared only ~11-21 kyr before a short eccentricity maximum, which confirms orbital phasing of the PETM CIE onset close to a short eccentricity maximum (Zachos et al., 2010).

3.3 Was the PETM close to a long eccentricity maximum?

Spectral analyses of Contessa Road records do not allow extraction of long eccentricity signals; however, AM and FM patterns of short eccentricity help to identify orbital phasing of the PETM CIE onset with respect to long eccentricity. AM of short eccentricity indicates that the PETM CIE onset appeared in the ascending flank of a long eccentricity cycle, close to a long eccentricity maximum (dashed red line in Fig. 5a, c, e). Irregular AM patterns of short eccentricity cycles between different Contessa Road records hinder accurate numerical estimation of the PETM CIE onset with respect to long eccentricity. Depth-domain EHA of filtered short eccentricity signals reveal that the PETM CIE onset coincided with positive interference of two short eccentricity components (E2 and E3; Fig. 6a-c), which is a common pattern of long eccentricity maxima (Laurin et al., 2016) that confirms orbital phasing of the PETM CIE onset close to a long eccentricity maximum.

Age-domain EHA of detrended Contessa Road records reveal two short eccentricity components (E2 and E3; Fig. 6d-f) that allow identification of negative interference ~200-300 kyr after the PETM onset (Fig. 6d-f). Recognition of the long eccentricity minimum associated with these FM patterns is hindered by signal distortion, which is likely related to enhanced $CaCO_3$ sedimentation following the PETM $CaCO_3$ dissolution interval (Kelly et al., 2010; Luo et al., 2016; Penman et al., 2016). In contrast, well-developed negative interference of E2-E3 components before the PETM allow better recognition of long eccentricity minima. Bifurcations of short eccentricity components reveal a long eccentricity minimum between ~-170 and ~-240 kyr (Fig. 6d-f), which indicates a long eccentricity maximum between ~-40 and ~30 kyr at Contessa Road. The PETM CIE onset at Contessa Road occurred close to the center of a long junction of E2 and E3 components in the range of a long eccentricity maximum, which implies that the PETM CIE onset occurred close to a long eccentricity maximum (Lourens et al., 2005; Zeebe and Lourens, 2019).

Precession-based age models for the ODP Site 1262 a* and Fe records were developed to estimate numerically orbital phasing of the PETM CIE onset with respect to long eccentricity (*see Supplementary information*). These records were used previously to develop astrochronological age models for ODP Site 1262 (Westerhold et al., 2007, 2018); however, those chronologies assumed a ~120 kyr PETM $CaCO_3$ dissolution interval duration. The ~116-137 kyr PETM $CaCO_3$ dissolution interval duration estimate from Contessa Road reveals that extensive $CaCO_3$ dissolution should have lasted for longer in deep ocean sites– i.e., ODP Site 1262. Although this assumption requires further research due to the different paleogeographic positions of Contessa Road and ODP Site 1262 (Fig. 1c), different estimates of 170 ± 30 kyr and $167^{+32}/_{-24}$ kyr for the PETM $CaCO_3$ dissolution interval at South Atlantic sites validate the inference that extensive $CaCO_3$ dissolution at ODP Site 1262 may have lasted longer than ~120 kyr (Murphy et al., 2010; Zeebe and Lourens, 2019). This suggests that the ODP 1262 astrochronological age model can be refined.

Precession-based chronologies for ODP Site 1262 a* and Fe records allow identification of long eccentricity signals in power spectra (*see Supplementary information*). Filtered long eccentricity signals of the ODP Site 1262 a* and Fe records are now separated by the 170 ± 30 kyr PETM $CaCO_3$ dissolution interval which refines the precession-based age model for this site. Long eccentricity signals have good visual correlation with detrended records (Fig. 7). However, these signals do not provide a unique estimate for the long eccentricity maximum of the cycle that contains the PETM (cycle 0 in Fig. 7) because this cycle is punctuated by the PETM $CaCO_3$ dissolution interval.

The filtered long eccentricity signal of the a* record enables identification of a long eccentricity maximum at ~-33 kyr for cycle 0 (blue circle in Fig. 7a). However, a long eccentricity minimum at ~-227 kyr for cycle 0 indicates a long eccentricity maximum at ~-25 kyr. The long eccentricity maximum of cycle -1, which preceded the PETM CIE onset appeared at ~-419 kyr, which implies a long eccentricity maximum at ~-14 kyr for cycle 0 (Fig. 7a). Filtered long eccentricity signals of the a* record indicate a long eccentricity minimum at ~200 kyr, which suggest that the long eccentricity maximum of cycle 0 appeared at ~-3 kyr. Considering the ±30 kyr uncertainty of the PETM $CaCO_3$ dissolution interval at

ODP Site 1262, this estimate for the age of the long eccentricity maximum of cycle 0 ranges between ~-33 kyr and ~28 kyr (Fig. 7a). A similar estimate can be obtained using the long eccentricity maximum of cycle 1, which appeared at ~400 ± 30 kyr (considering the uncertainty of the PETM $CaCO_3$ dissolution interval) and reveals a long eccentricity maximum for cycle 0 at -5 ± 30 kyr. All of these values, after probabilistic assessments (*see Supplementary information*), produce a -11 ± 15 kyr (median and 95% confidence interval) estimate for the age of the long eccentricity maximum of cycle 0 in the floating chronology of the a* record (Fig. 7a).

The filtered long eccentricity signal of the Fe record can also be used to estimate the age of the long eccentricity maximum of cycle 0. These estimates, however, are limited by poor development of the long eccentricity minimum of cycle 1 after the PETM $CaCO_3$ dissolution interval (Fig. 7b). The filtered long eccentricity signal of the Fe record reveals a long eccentricity maximum at ~-13 kyr (blue circle in cycle 0; Fig. 7b). However, cycle 0 has a well-developed long eccentricity minimum at ~-209 kyr, which indicates a long eccentricity maximum at ~-7 kyr. The long eccentricity maximum of cycle -1, which precedes cycle 0, appeared at ~-407 kyr (Fig. 7b), which allows identification of a long eccentricity maximum at ~-2 kyr for cycle 0. Alternatively, the long eccentricity maximum of cycle 1 at -364 ± 30 kyr (considering the uncertainty of the PETM $CaCO_3$ dissolution interval; Fig. 7b) indicates a long eccentricity maximum at -41 ± 30 kyr. Estimates of the long eccentricity maximum of cycle 0 in the Fe record reveal lags between the a* and Fe records. These differences, which are also identified in previous cyclostratigraphic framewords (Westerhold et al., 2007), may be associated with terrigenous material input shifts promoted by hydrological cycle variations under global warming (e.g., Woodard et al., 2011; Jin et al., 2021). However, estimates of the long eccentricity maximum of cycle 0 for both records are similar (Fig. 7). Combined estimates of the age of the long eccentricity maximum of cycle 0 in the Fe record (*see Supplementary information*) produce a -24 ± 19 kyr age estimate for this long eccentricity maximum (Fig. 7b).

Our estimates of the orbital phasing of the PETM coincide with those from the ZB18a astronomical solution (Zeebe and Lourens, 2019). In the ZB18a astronomical solution, the PETM CIE onset occurred at 56.01 ± 0.05 Ma and a long eccentricity maximum appeared at ~56.04 Ma. These overlapping estimates confirm that the PETM was an orbitally paced event (Lourens et al., 2005; Zeebe and Lourens, 2019). This evidence implies that the orbitally controlled mechanism that promoted early Eocene light carbon releases may have also been activated at the Paleocene/Eocene boundary (Lunt et al., 2011; DeConto et al., 2012; Kirtland Turner et al., 2014). This mechanism depended strongly on early Eocene long-term background temperatures, which are interpreted to have been higher than pre-PETM temperatures (Fig. 1a; Westerhold et al., 2020). Therefore, crossing of a thermodynamic threshold and subsequent destabilization of carbon reservoirs at the PETM onset may have required an exceptionally large temperature increase. Volcanic-related positive carbon cycle feedbacks before the PETM CIE onset promoted temperature increases (Sluijs et al., 2007; Frieling et al., 2019; Kender et al., 2021). These processes coincided with orbital phasing of the PETM CIE onset close to both long and short eccentricity maxima. This indicates an orbital configuration that produced persistently high eccentricity values with minimal variation across the time interval during which the PETM CIE onset occurred (Laskar et al., 2004; Zeebe et al., 2017; Zeebe and Lourens, 2019). Maximal seasonal contrast associated with both long and short eccentricity maxima may have promoted a larger temperature increase than may have occurred with only volcanic-related carbon emissions. Increased temperatures, and associated ocean circulation changes due to global warming, may have led the climate to cross a thermodynamic threshold that produced light carbon injections due to thermal destabilization of methane hydrates (Lunt et al., 2011). This scenario is compatible with orbital control on the PETM CIE onset, as our data indicate; however, other processes associated with organic carbon feedbacks may have also been involved in PETM CIE triggering. Orbitally controlled temperature increases may have accelerated decomposition of soil organic carbon from terrestrial permafrost (DeConto et al., 2012). Although light carbon releases produced by this mechanism may have occurred, evidence for major Paleocene-Eocene permafrost soil carbon stocks is controversial; therefore, disturbed biospheric carbon stocks, and light carbon releases associated with decomposed terrestrial organic matter due to global warming in diverse latitudes have been suggested to play a role in PETM CIE triggering (Bowen, 2013). Any of these carbon reservoirs may have been destabilized by a drastic orbitally controlled and volcanic-related temperature increase that triggered the initial PETM light carbon release.

5. Conclusions

AM and FM patterns provide evidence in a relative sense, i.e., independent of absolute orbital tuning and astronomical solutions, that the PETM CIE commenced close to both long and short eccentricity maxima. Orbital signatures within Contessa Road pelagic carbonates indicate that this event occurred ~11-21 kyr before a short eccentricity maximum, which confirms the orbital phasing of the PETM close to a short eccentricity maximum (Zachos et al., 2010). Orbital forcing of short eccentricity played a central role in lysocline depth fluctuations at Contessa Road. This produced PETM sedimentation patterns similar to those of other early Eocene carbon cycle perturbations such as the ETM 2 and H2 events (Galeotti et al., 2010; Zachos et al., 2010).

FM patterns from Contessa Road and precession-based age models from ODP Site 1262 reveal that the PETM CIE onset occurred close to a long eccentricity maximum. This evidence indicates that the PETM was an orbitally paced event that was, at least, partially triggered by an orbitally controlled mechanism. Similarities between the orbital phasing of the PETM and other early Eocene carbon cycle perturbations suggest that these events were driven by a common mechanism that produced light carbon releases from a carbon reservoir that was thermally destabilized–i.e., methane hydrates, permafrost soil, and/or other terrestrial organic matter. Maximal seasonal contrast of the orbital configuration in which the PETM occurred, and volcanic-related positive carbon cycle feedbacks may have triggered the PETM CIE and contributed to the exceptionally large PETM magnitude.

ACKNOWLEDGEMENTS

This work was supported financially by the Colfuturo Foundation and the Australian National University through scholarships to V.A.P., by the Dipartimento di Scienze Pure e Applicate, University of Urbino (to S.G.), by the Institute for Climate Change Solutions (to S.G. and F.F.), by the Australian Research Council (grants DP190100874 to A.P.R. and D.H.; DE190100042 to K.M.G.), by the Istituto Nazionale di Geofisica e Vulcanologia (to F.F.), by the U.S. National Science Foundation (grants OCE20-01022 and OCE20-34660 to R.E.Z.), and by the Heising-Simons Foundation (Grant #2021-2800 to R.E.Z.). We thank two anonymous reviewers and the editor, Andrew Jacobson, for their comments that improved this paper.

References

Aguirre-Palafox, L. E., Alvarez, W., Boschi, S., Martin, E., Schmitz, B., 2019. Zircon provenance analysis from Lower Paleocene pelagic limestones of the Bottaccione section at

Gubbio (Umbria-Marche basin, Italy), in: Koeberl, C., Bice, D. M. (Eds.), 250 Million Years of Earth History in Central Italy: Celebrating 25 Years of the Geological Observatory of Coldigioco. Geological Society of America Special Paper 542. pp. 159-174. https://doi.org/10.1130/2019.2542(08).

Aziz, H. A., Hilgen, F. J., van Luijk, G. M., Sluijs, A., Kraus, M. J., Pares, J. M., Gingerich, P. D., 2008. Astronomical climate control on paleosol stacking patterns in the upper Paleocene-lower Eocene Willwood Formation, Bighorn Basin, Wyoming. Geology 36, 531-534. https://doi.org/10.1130/G24734A.1.

Berger, A., Loutre, M. F., 1991. Insolation values for the climate of the last 10 million years. Quat. Sci. Rev. 10, 297-317. https://doi.org/10.1016/0277-3791(91)90033-q.

Bowen, G. J., 2013. Up in smoke: a role for organic carbon feedbacks in Paleogene hyperthermals. Global Planet. Change 109, 18-29. https://doi.org/10.1016/j.gloplacha.2013.07.001.

Coccioni, R., Frontalini, F., Catanzariti, R., Jovane, L., Rodelli, D., Rodrigues, I. M., Savian, J. F., Giorgioni, M., Galbrun, B., 2019. Paleoenvironmental signature of the Selandian-Thanetian transition event (STTE) and Early Late Paleocene Event (ELPE) in the Contessa Road section (western Neo-Tethys). Palaeogeogr. Palaeoclimatol. Palaeoecol. 523, 62-77. https://doi.org/10.1016/j.palaeo.2019.03.023.

Cramer, B. S., Wright, J. D., Kent, D. V., Aubry, M.-P., 2003. Orbital climate forcing of $\delta^{13}C$ excursions in the late Paleocene–early Eocene (chrons C24n–C25n). Paleoceanography 18, 1097. https://doi.org/10.1029/2003PA000909.

DeConto, R. M., Galeotti, S., Pagani, M., Tracy, D., Schaefer, K., Zhang, T., Pollard, D., Beerling, D. J., 2012. Past extreme warming events linked to massive carbon release from thawing permafrost. Nature 484, 87-91. https://doi.org/10.1038/nature10929.

Francescone, F., Lauretano, V., Bouligand, C., Moretti, M., Sabatino, N., Schrader, C., Catanzariti, R., Hilgen, F., Lanci, L., Turtù, A., Sprovieri, M., Lourens, L., Galeotti, S., 2018. A 9 million-year-long astrochronological record of the early- middle Eocene corroborated by seafloor spreading rates. Bull. Geol. Soc. Am. 131, 499-520, https://doi.org/10.1130/B32050.1

Frieling, J., Svensen, H. H., Planke, S., Cramwinckel, M. J., Selnes, H., Sluijs, A., 2016. Thermogenic methane release as a cause for the long duration of the PETM. Proc. Natl Acad. Sci. USA 113, 12059-12064. https://doi.org/10.1073/pnas.1603348113.

Frieling, J., Peterse, F., Lunt, D. J., Bohaty, S. M., Sinninghe Damsté, J. S., Reichart, G.-J., Sluijs, A., 2019. Widespread warming before and elevated barium burial during the Paleocene-Eocene Thermal Maximum: evidence for methane hydrate release? Paleoceanogr. Paleoclimatol. 34, 546-566. https://doi.org/10.1029/2018PA003425.

Galeotti, S., Angori, E., Coccioni, R., Ferrari, G., Galbrun, B., Monechi, S., Premoli Silva, I., Speijer, R., Turi, B., 2000. Integrated stratigraphy across the Paleocene/Eocene boundary in the Contessa Road section, Gubbio (central Italy). Bull. Soc. Geol. France 171, 355-365. https://doi.org/10.2113/171.3.355.

Galeotti, S., Krishnan, S., Pagani, M., Lanci, L., Gaudio, A., Zachos, J. C., Monechi, S., Morelli, G., Lourens, L., 2010. Orbital chronology of early Eocene hyperthermals from the Contessa Road section, central Italy. Earth Planet. Sci. Lett. 290, 192-200. https://doi.org/10.1016/j.epsl.2009.12.021.

Giusberti, L., Coccioni, R., Sprovieri, M., Tateo, F., 2009. Perturbation at the sea floor during the Paleocene-Eocene Thermal Maximum: evidence from benthic foraminifera at Contessa Road, Italy. Mar. Micropaleontol. 70, 102-119. https://doi.org/10.1016/j.marmicro.2008.11.003.

Husson, D., 2014. MathWorks File Exchange: RedNoise_ConfidenceLevels. https://www.mathworks.com/matlabcentral/fileexchange/45539-rednoise_confidencelevels.

Jin, S., Kemp, D. B., Jolley, D. W., Vieira, M., Zachos, J. C., Huang, C., Li, M., Chen, W., 2022. Large-scale, astronomically paced sediment input to the North Sea Basin during the Paleocene Eocene Thermal Maximum. Earth Planet. Sci. Lett. 579, 117340. https://doi.org/10.1016/j.epsl.2021.117340.

Kelly, D. C., Nielsen, T. M., McCarren, H. K., Zachos, J. C., Röhl, U., 2010. Spatiotemporal patterns of carbonate sedimentation in the South Atlantic: implications for carbon cycling during the Paleocene-Eocene thermal maximum. Palaeogeogr. Palaeoclimatol. Palaeoecol. 293, 30-40. https://doi.org/10.1016/j.palaeo.2010.04.027.

Kender, S., Bogus, K., Pedersen, G. K., Dybkjær, K., Mather, T. A., Mariani, E., Ridgwell, A., Riding, J. B., Wagner, T., Hesselbo, S. P., Leng, M. J., 2021. Paleocene/Eocene carbon feedbacks triggered by volcanic activity. Nat. Commun. 12, 1-10. https://doi.org/10.1038/s41467-021-25536-0.

Kirtland Turner, S., Sexton, P. F., Charles, C. D., Norris, R. D., 2014. Persistence of carbon release events through the peak of early Eocene global warmth. Nat. Geosci. 7, 748-751. https://doi.org/10.1038/ngeo2240.

Laskar, J., Robutel, P., Joutel, F., Gastineau, M., Correia, A. C. M., Levrard, B., 2004. A long-term numerical solution for the insolation quantities of the Earth. Astron. Astrophys. 428, 261-285. https://doi.org/10.1051/0004-6361:20041335.

Laurin, J., Meyers, S. R., Sageman, B. B., Waltham, D., 2005. Phase-lagged amplitude modulation of hemipelagic cycles: a potential tool for recognition and analysis of sea-level change. Geology 33, 569-572. https://doi.org/10.1130/G21350.1.

Laurin, J., Meyers, S. R., Galeotti, S., Lanci, L., 2016. Frequency modulation reveals the phasing of orbital eccentricity during Cretaceous Oceanic Anoxic Event II and the Eocene hyperthermals. Earth Planet. Sci. Lett. 442, 143-156. https://doi.org/10.1016/j.epsl.2016.02.047.

Laurin, J., Uličný, D., Čech, S., Trubač, J., Zachariáš, J., Svobodová, A., 2021. Chronology and eccentricity phasing for the Early Turonian greenhouse (~93–94 Ma): constraints on astronomical control of the carbon cycle. Paleoceanogr. Paleoclimatol. 36, e2020PA004188. https://doi.org/10.1029/2020PA004188.

Li, M., Hinnov, L., Kump, L., 2019. Acycle: time-series analysis software for paleoclimate research and education. Comput. Geosci. 127, 12-22. https://doi.org/10.1016/j.cageo.2019.02.011.

Lourens, L. J., Sluijs, A., Kroon, D., Zachos, J. C., Thomas, E., Röhl, U., Bowles, J., Raffi, I., 2005. Astronomical pacing of late Palaeocene to early Eocene global warming events. Nature 435, 1083-1087, https://doi.org/10.1038/nature03814.

Luo, Y., Boudreau, B. P., Dickens, G. R., Sluijs, A., Middelburg, J. J., 2016. An alternative model for $CaCO_3$ over-shooting during the PETM: biological carbonate compensation. Earth Planet. Sci. Lett. 453, 223-233. https://doi.org/10.1016/j.epsl.2016.08.012.

Lunt, D. J., Ridgwell, A., Sluijs, A., Zachos, J., Hunter, S., Haywood, A., 2011. A model for orbital pacing of methane hydrate destabilization during the Palaeogene. Nat. Geosci. 4, 775-778. https://doi.org/10.1038/ngeo1266.

Lyons, S. L., Baczynski, A. A., Babila, T. L., Bralower, T. J., Hajek, E. A., Kump, L. R., Polites, E. G., Self-Trail, J. M., Trampush, S. M., Vornlocher, J. R., Zachos, J. C., Freeman, K. H., 2019. Palaeocene-Eocene Thermal Maximum prolonged by fossil carbon oxidation. Nat. Geosci. 12, 54-60. https://doi.org/10.1038/s41561-018-0277-3.

Mann, M. E., Lees, J. M., 1996. Robust estimation of background noise and signal detection in climatic time series. Clim. Change 33, 409-445. https://doi.org/10.1007/BF00142586.

Meyers, S. R., Sageman, B. B., Hinnov, L. A., 2001. Integrated quantitative stratigraphy of the Cenomanian-Turonian Bridge Creek Limestone Member using evolutive harmonic analysis and stratigraphic modelling. J. Sediment. Res. 71, 628-644. https://doi.org/10.1306/012401710628.

Meyers, S. R., 2015. The evaluation of eccentricity-related amplitude modulation and bundling in paleoclimate data: an inverse approach for astrochronologic testing and time scale optimization. Paleoceanography 30, 1625-1640. https://doi.org/10.1002/2015PA002850.

Murphy, B. H., Farley, K. A., Zachos, J. C., 2010. An extraterrestrial ^{3}He-based timescale for the Paleocene-Eocene thermal maximum (PETM) from Walvis Ridge, IODP Site 1266. Geochim. Cosmochim. Acta 74, 5098-5108. https://doi.org/10.1016/j.gca.2010.03.039.

Penman, D. E., Kirtland Turner, S., Sexton, P. F., Norris, R. D., Dickson, A. J., Boulila, S., Ridgwell, A., Zeebe, R. E., Zachos, J. C., Cameron, A., Westerhold, T., Röhl, U., 2016. An abyssal carbonate compensation depth overshoot in the aftermath of the Palaeocene-Eocene Thermal Maximum. Nat. Geosci. 9, 575-580. https://doi.org/10.1038/ngeo2757.

Pogge von Strandmann, P. A., Jones, M. T., West, A. J., Murphy, M. J., Stokke, E. W., Tarbuck, G., Wilson, D. J., Pearce, C. R., Schmidt, D. N., 2021. Lithium isotope evidence for enhanced weathering and erosion during the Paleocene-Eocene Thermal Maximum. Sci. Adv. 7, p.eabh4224. https://doi.org/10.1126/sciadv.abh4224.

Rial, J. A., 1999. Pacemaking the ice ages by frequency modulation of Earth’s orbital eccentricity. Science 285, 564-568. https://doi.org/10.1126/science.285.5427.564.

Röhl, U., Bralower, T. J., Norris, R. D., Wefer, G., 2000. New chronology for the late Paleocene thermal maximum and its environmental implications. Geology 28, 927-930. https://doi.org/10.1130/0091-7613(2000)28<927:NCFTLP>2.0.CO;2.

Röhl, U., Westerhold, T., Bralower, T. J., Zachos, J. C., 2007. On the duration of the Paleocene-Eocene thermal maximum (PETM). Geochem. Geophys. Geosyst. 8, Q12002. https://doi.org/10.1029/ 2007GC001784.

Sluijs, A., Brinkhuis, H., Schouten, S., Bohaty, S. M., John, C. M., Zachos, J. C., Reichart, G. -J., Sinninghe Damsté, J. S., Crouch, E. M., Dickens, G. R., 2007. Environmental precursors to rapid light carbon injection at the Palaeocene/Eocene boundary. Nature 450, 1218-1221. https://doi.org/10.1038/nature06400.

Svensen, H., Planke, S., Malthe-Sørenssen, A., Jamtveit, B., Myklebust, R., Eidem, T. R., Rey, S. S., 2004. Release of methane from a volcanic basin as a mechanism for initial Eocene global warming. Nature 429, 542-545. https://doi.org/10.1038/nature02566.

van der Meulen, B., Gingerich, P. D., Lourens, L. J., Meijer, N., van Broekhuizen, S., van Ginneken, S., Abels, H. A., 2020. Carbon isotope and mammal recovery from extreme greenhouse warming at the Paleocene-Eocene boundary in astronomically-calibrated fluvial strata, Bighorn Basin, Wyoming, USA. Earth Planet. Sci. Lett. 534, 116044. https://doi.org/10.1016/j.epsl.2019.116044.

Westerhold, T., Röhl, U., Laskar, J., Raffi, I., Bowles, J., Lourens, L. J., Zachos, J. C., 2007. On the duration of magnetochrons C24r and C25n and the timing of early Eocene global warming events: implications from the Ocean Drilling Program Leg 208 Walvis Ridge depth transect. Paleoceanography 22, PA2201. https://doi.org/10.1029/2006PA001322.

Westerhold, T., Röhl, U., Wilkens, R. H., Gingerich, P. D., Clyde, W. C., Wing, S. L., Bowen, G. J., Kraus, M. J., 2018. Synchronizing early Eocene deep-sea and continental records-cyclostratigraphic age models for the Bighorn Basin Coring Project drill cores. Clim. Past 14. 303-319. https://doi.org/10.5194/cp-14-303-2018.

Westerhold, T., Marwan, N., Drury, A. J., Liebrand, D., Agnini, C., Anagnostou, E., Barnet, J. S. K., Bohaty, S. M., De Vleeschouwer, D., Florindo, F., Frederichs, T., Hodell, D. A., Holbourn, A. E., Kroon, D., Lauretano, V., Littler, K., Lourens, L. J., Lyle, M., Pälike, H., Röhl, U., Tian, J., Wilkens, R. H., Wilson, P. A., Zachos, J. C., 2020. An astronomically dated record of Earth's climate and its predictability over the last 66 million years. Science 369, 1383-1387. https://doi.org/10.1126/science.aba6853.

Woodard, S. C., Thomas, D. J., Hovan, S., Röhl, U., Westerhold, T., 2011. Evidence for orbital forcing of dust accumulation during the early Paleogene greenhouse. Geochem. Geophys. Geosyst. 12, Q02007. https://doi.org/10.1029/2010GC003394.

Zachos, J. C., Röhl, U., Schellenberg, S. A., Sluijs, A., Hodell, D. A., Kelly, D. C., Thomas, E., Nicolo, M., Raffi, I., Lourens, L. J., McCarren, H., Kroon, D., 2005. Rapid acidification of the ocean during the Paleocene-Eocene Thermal Maximum. Science 308, 1611-1615. https://doi.org/10.1126/science.1109004.

Zachos, J. C., McCarren, H., Murphy, B., Röhl, U., Westerhold, T., 2010. Tempo and scale of late Paleocene and early Eocene carbon isotope cycles: implications for the origin of hyperthermals. Earth Planet. Sci. Lett. 299, 242-249. https://doi.org/10.1016/j.epsl.2010.09.004.

Zeebe, R. E., Zachos, J. C., Dickens, G. R., 2009. Carbon dioxide forcing alone insufficient to explain Palaeocene-Eocene Thermal Maximum warming. Nat. Geosci. 2, 576-580. https://doi.org/10.1038/ngeo578.

Zeebe, R. E., 2013. What caused the long duration of the Paleocene-Eocene Thermal Maximum? Paleoceanography 28, 440-452. https://doi.org/10.1002/palo.20039.

Zeebe, R. E., Westerhold, T., Littler, K., Zachos, J. C., 2017. Orbital forcing of the Paleocene and Eocene carbon cycle. Paleoceanography 32, 440-465. https://doi.org/10.1002/2016PA003054.

Zeebe, R. E., Lourens, L. J., 2019. Solar System chaos and the Paleocene-Eocene boundary age constrained by geology and astronomy. Science 365, 926-929. https://doi.org/10.1126/science.aax0612.

Figure captions

Fig. 1. (a) Model results of orbital variations (forcing) with imposed long-term global temperature trends. Hyperthermals are represented by temperature peaks that cross a thermodynamic threshold (black dashed line) (Kirtland Turner et al., 2014). (b) ODP Site 1262 $CaCO_3$ record indicating the PETM $CaCO_3$ dissolution interval. (c) Paleogeographic reconstruction at ~56 Ma (Pogge von Strandmann et al., 2021) with locations of the Contessa Road section and ODP Site 1262. (d) Paleogeographic reconstruction of sedimentary environments across the western Tethys Ocean (Aguirre-Palafox et al., 2019).

Fig. 2. (a) Schematic stratigraphic summary of the Contessa Road through the interval 26-46 m above the K/Pg boundary. The purple rectangle indicates the studied outcrop interval. (b) Lithological variations in the studied Contessa Road outcrop interval (Giusberti et al., 2009; Galeotti et al., 2010). (c) $CaCO_3$ record (Giusberti et al., 2009). (d) $\delta^{13}C$ record (Giusberti et al., 2009). Elemental concentration records and EHA for (e) $Log_{10}Fe$, (f) Ca, and (g) $Log_{10}Si$. Dashed white lines in EHA plots indicate wavelength component variability. EHA were obtained using 80 cm sliding windows that move in 1 cm steps for the means of the $Log_{10}Fe$, Ca, and $Log_{10}Si$ records. Pre-marly, marly, and post-marly intervals are indicated. The marly interval represents the PETM $CaCO_3$ dissolution interval at Contessa Road. Gray rectangles define marly horizons. The rest of the sequence consists of limestones. The PETM CIE onset is indicated by a dashed green line in all plots.

Fig. 3. $Log_{10}Fe$, Ca, and $Log_{10}Si$ power spectra for the (a) whole section, (b) pre-marly, (c) marly, and (d) post-marly intervals at Contessa Road. Color bands represent frequency ranges that contain orbital signatures. Average periods for each orbital signature are also indicated.

Fig. 4. Filtered orbital signals for the Contessa Road sequence, including (a) $Log_{10}Fe$, (b) Ca, and (c) $Log_{10}Si$. Detrended data (gray) correlate well with filtered short eccentricity (green) and filtered precession (purple) signals.

Fig. 5. Filtered orbital signatures for Contessa Road (a, b) $Log_{10}Fe$, (c, d) Ca, and (e, f) $Log_{10}Si$. Short eccentricity (gray) and precession (blue) are presented in terms of mean and standard error (SE). AM of precession and short eccentricity are indicated by dashed purple and dashed red lines, respectively. EHA plots were generated using the filtered precession signals with 30 cm sliding windows that move in 1 cm steps. P1 and P2 correspond to precession components. Precession cycles are numbered. Marly horizons are pink shaded rectangles. The rest of the sequence consists of limestones. The PETM CIE onset is indicated by a dashed green line.

Fig. 6. Depth-domain EHA for filtered short eccentricity signals from Contessa Road (a) $Log_{10}Fe$, (b) Ca, and (c) $Log_{10}Si$. Depth-domain EHA were obtained using 150 cm sliding windows that move in 5 cm steps. Age-domain EHA of detrended records for Contessa Road (d) $Log_{10}Fe$, (e) Ca, and (f) $Log_{10}Si$. Age-domain EHA were obtained using 250 kyr sliding windows that move in 2.5 kyr steps. Records were set to 0 kyr at the PETM CIE onset (i.e., negative ages correspond to pre-PETM ages). Short eccentricity components (E2 and E3), precession (P), and lithologies (right) are indicated. The PETM CIE onset is indicated by a white bar.

Fig. 7. Age-domain detrended records (gray) and filtered long eccentricity signals (blue) for ODP Site 1262 (a) a* and (b) $Log_{10}Fe$ records. Long eccentricity cycles are numbered. Cycle 0 contains the PETM. Black bars represent the 170 ± 30 kyr PETM $CaCO_3$ dissolution

interval duration, which separates the pre-PETM (Paleocene) and post-PETM (Eocene) intervals at this site. Records were set to 0 kyr at the PETM CIE onset (negative ages correspond to pre-PETM ages). Blue circles represent long eccentricity maxima of the filtered time-domain long eccentricity signals. Estimates of the age of the long eccentricity maximum of cycle 0 are indicated in fuchsia, in terms of median ± 95% confidence interval. The estimate for the age of the long eccentricity maximum of cycle 0 at Contessa Road is indicated in orange. All estimates coincide within uncertainties. The PETM CIE onset is indicated with a green dashed line.

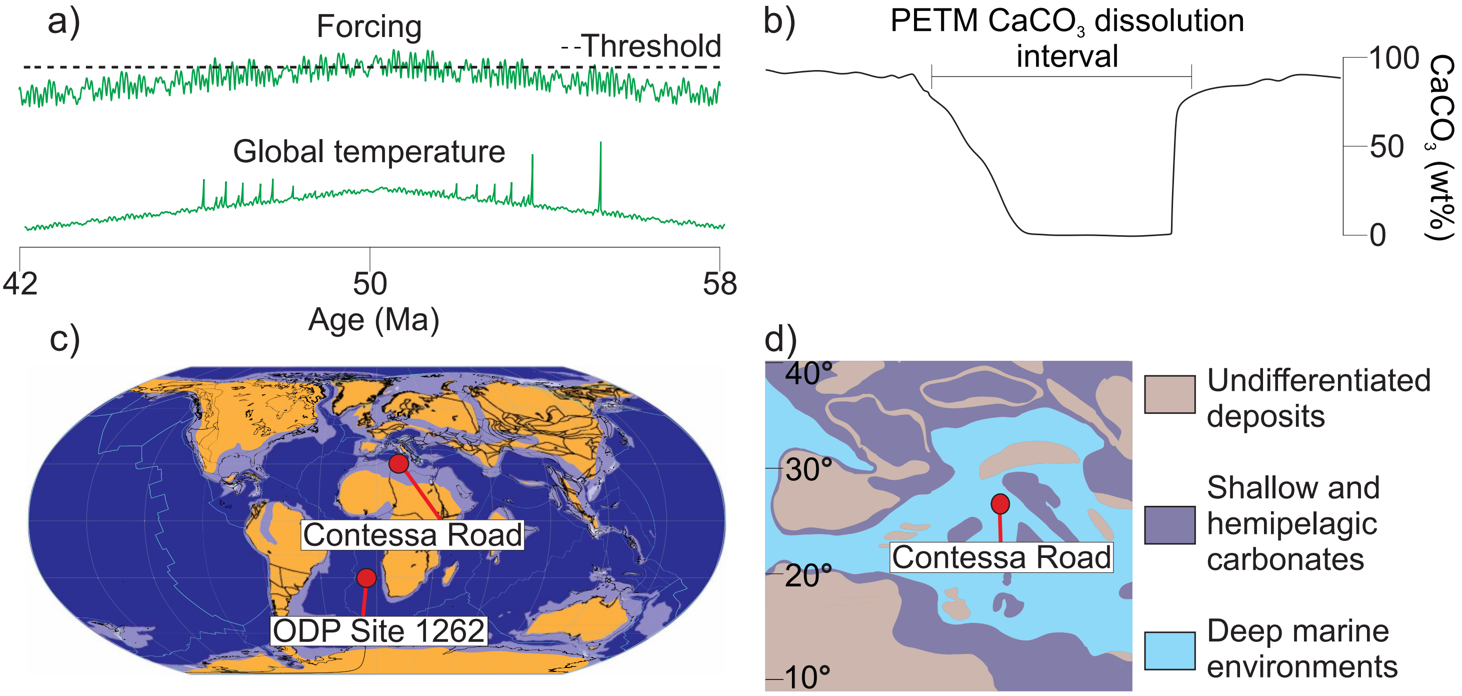
a)
Forcing
--Threshold
Global temperature
42
50
58
Age (Ma)
b)
PETM CaCO$_3$ dissolution interval
100
50
0
CaCO$_3$ (wt%)
c)
Contessa Road
ODP Site 1262
d)
40°
30°
20°
10°
Contessa Road
Undifferentiated deposits
Shallow and hemipelagic carbonates
Deep marine environments

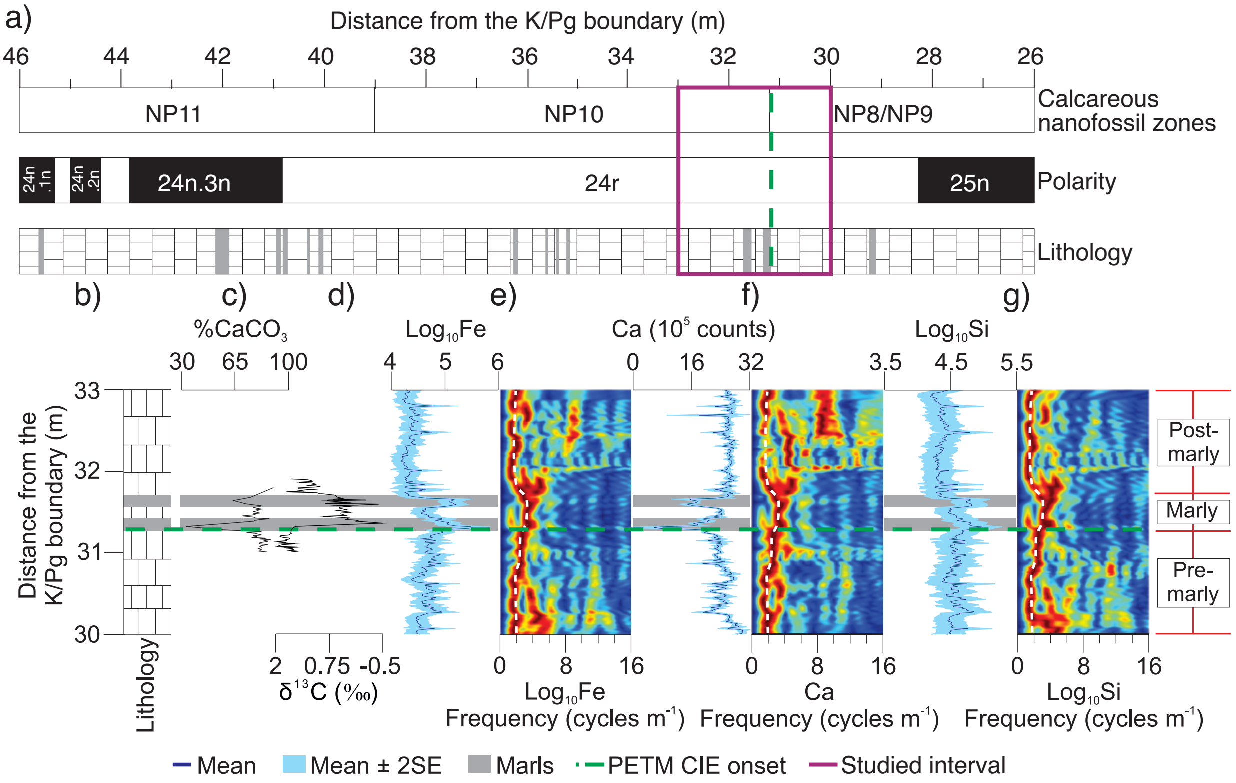
a)
Distance from the K/Pg boundary (m)
46
44
42
40
38
36
34
32
30
28
26
NP11
NP10
NP8/NP9
Calcareous nanofossil zones
24n.1n
24n.2n
24n.3n
24r
25n
Polarity
Lithology
b)
c)
d)
e)
f)
g)
%CaCO$_3$
30
65
100
Log$_{10}$Fe
4
5
6
Ca (10^5 counts)
0
16
32
Log$_{10}$Si
3.5
4.5
5.5
Distance from the K/Pg boundary (m)
33
32
31
30
Lithology
2
0.75
-0.5
δ^{13}C (‰)
0
8
16
Log$_{10}$Fe Frequency (cycles m^{-1})
Ca Frequency (cycles m^{-1})
Log$_{10}$Si Frequency (cycles m^{-1})
Post-marly
Marly
Pre-marly
Mean
Mean ± 2SE
Marls
PETM CIE onset
Studied interval

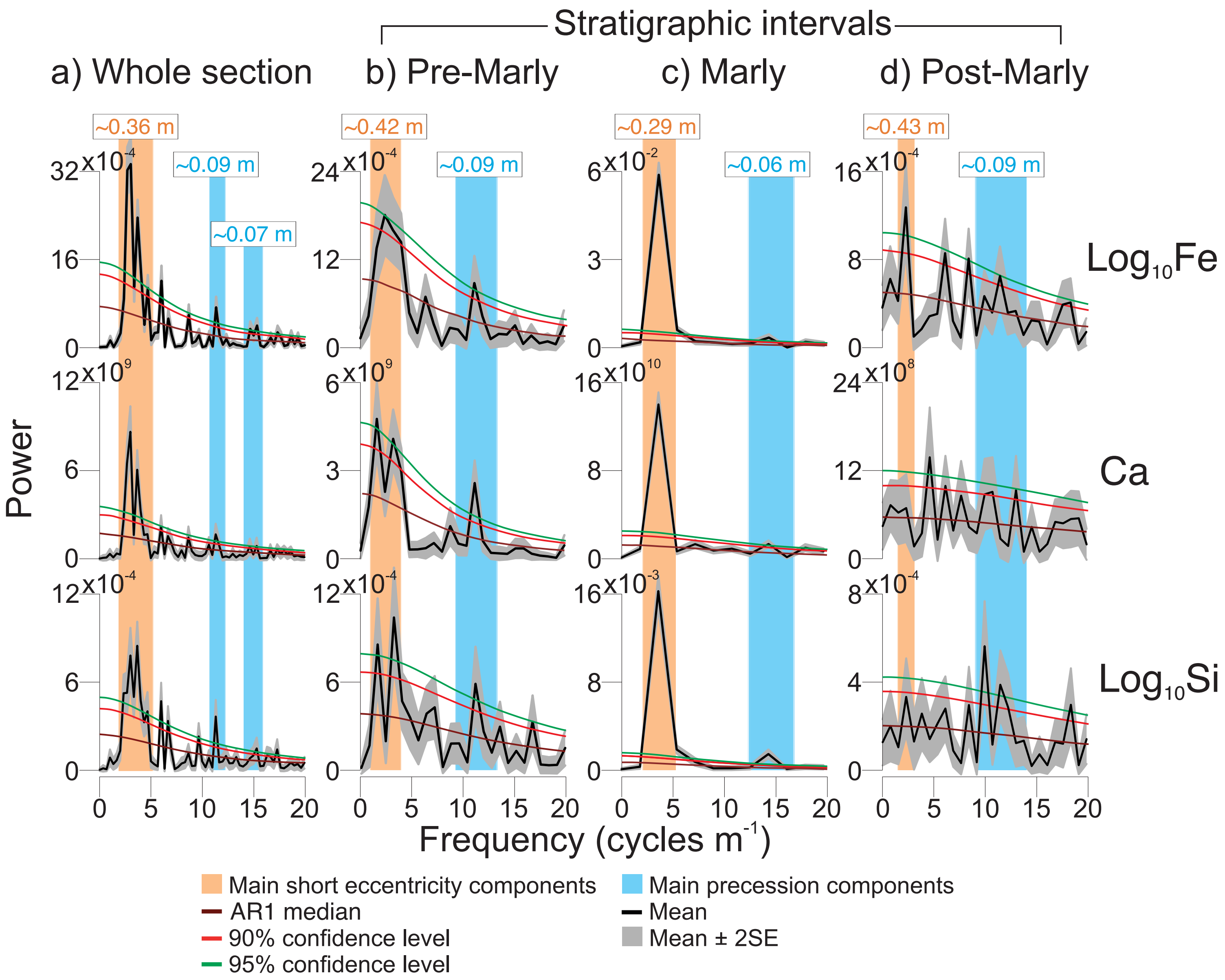
Stratigraphic intervals
a) Whole section
b) Pre-Marly
c) Marly
d) Post-Marly
~0.36 m
~0.09 m
~0.07 m
~0.42 m
~0.09 m
~0.29 m
~0.06 m
~0.43 m
~0.09 m
$Log_{10}Fe$
Ca
$Log_{10}Si$
Power
$x10^{-4}$
$x10^{9}$
$x10^{-4}$
$x10^{-4}$
$x10^{9}$
$x10^{-4}$
$x10^{-2}$
$x10^{10}$
$x10^{-3}$
$x10^{-4}$
$x10^{8}$
$x10^{-4}$
32
16
0
12
6
0
12
6
0
24
12
0
6
3
0
12
6
0
6
3
0
16
8
0
16
8
0
16
8
0
24
12
0
8
4
0
0 5 10 15 20
Frequency (cycles m^{-1})
Main short eccentricity components
AR1 median
90% confidence level
95% confidence level
Main precession components
Mean
Mean ± 2SE

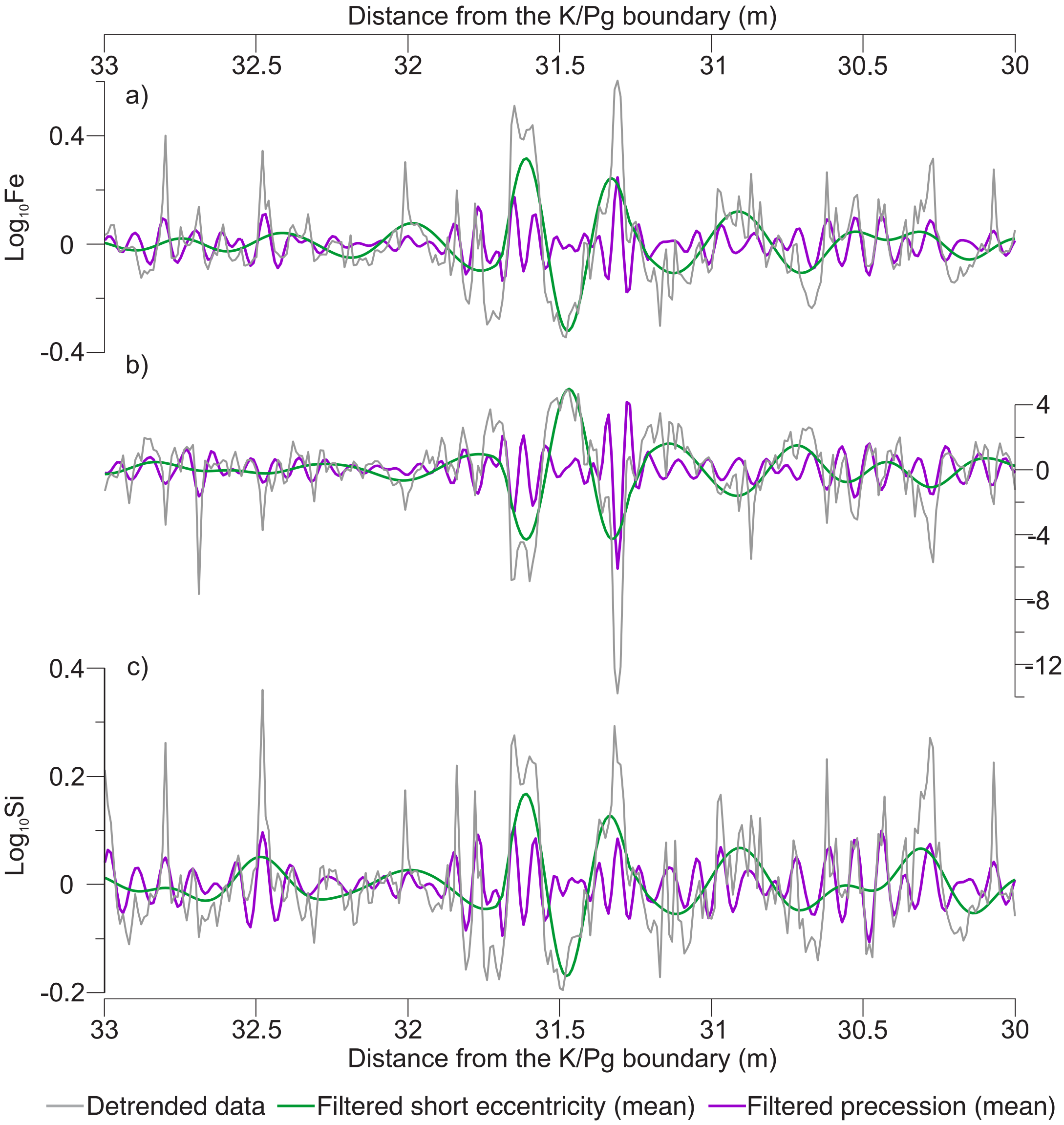
Distance from the K/Pg boundary (m)
33
32.5
32
31.5
31
30.5
30
a)
Log$_{10}$Fe
0.4
0
-0.4
b)
Ca (counts 10^5)
4
0
-4
-8
-12
c)
Log$_{10}$Si
0.4
0.2
0
-0.2
33
32.5
32
31.5
31
30.5
30
Distance from the K/Pg boundary (m)
Detrended data
Filtered short eccentricity (mean)
Filtered precession (mean)

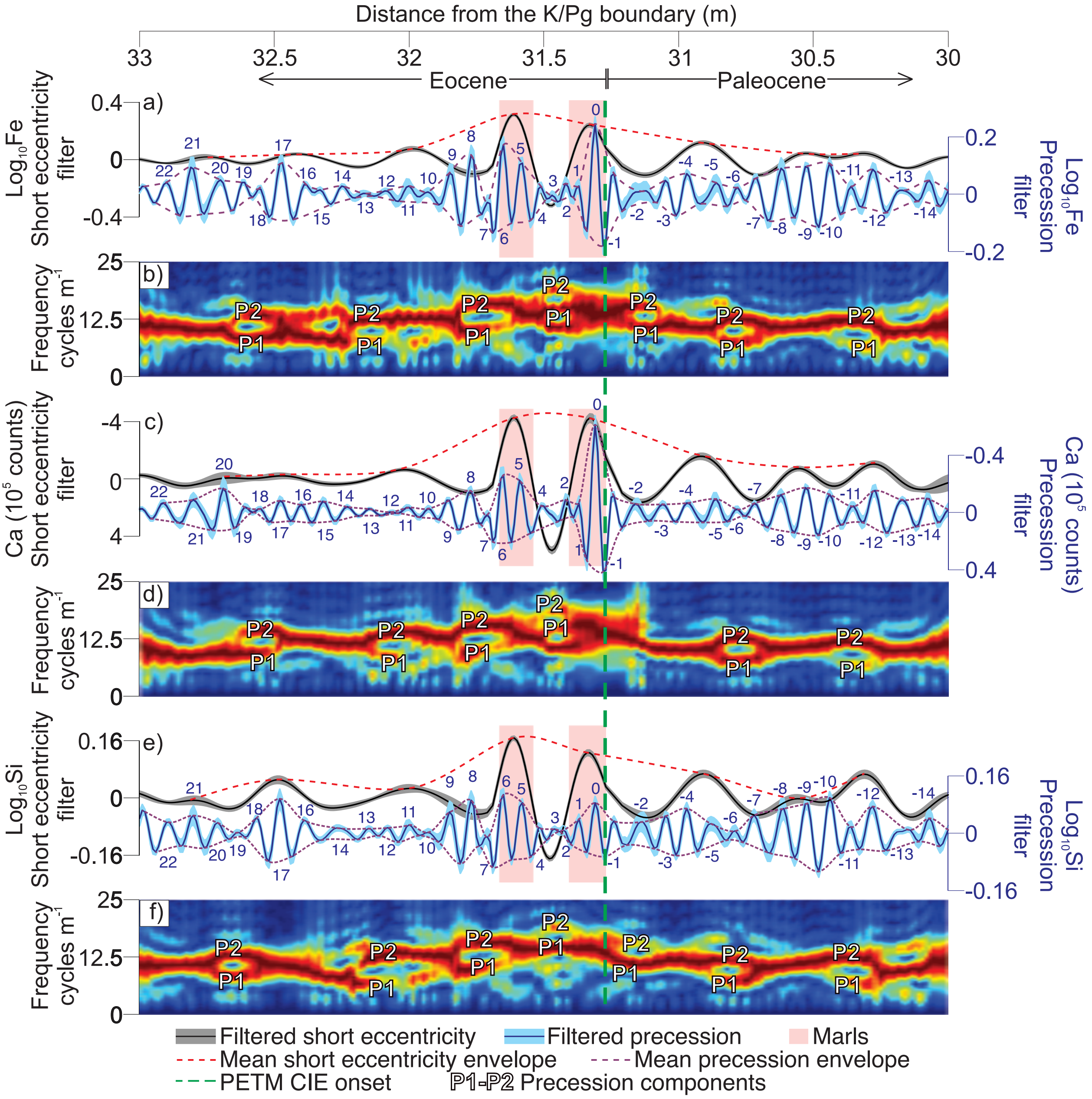
Distance from the K/Pg boundary (m)
33
32.5
32
31.5
31
30.5
30
Eocene
Paleocene
a)
Log$_{10}$Fe Short eccentricity filter
0.4
0
-0.4
Log$_{10}$Fe Precession filter
0.2
0
-0.2
b)
Frequency cycles m^{-1}
25
12.5
0
P2
P1
c)
Ca (10^5 counts) Short eccentricity filter
-4
0
4
Ca (10^5 counts) Precession filter
-0.4
0
0.4
d)
e)
Log$_{10}$Si Short eccentricity filter
0.16
0
-0.16
Log$_{10}$Si Precession filter
0.16
0
-0.16
f)
Filtered short eccentricity
Filtered precession
Marls
Mean short eccentricity envelope
Mean precession envelope
PETM CIE onset
P1-P2 Precession components

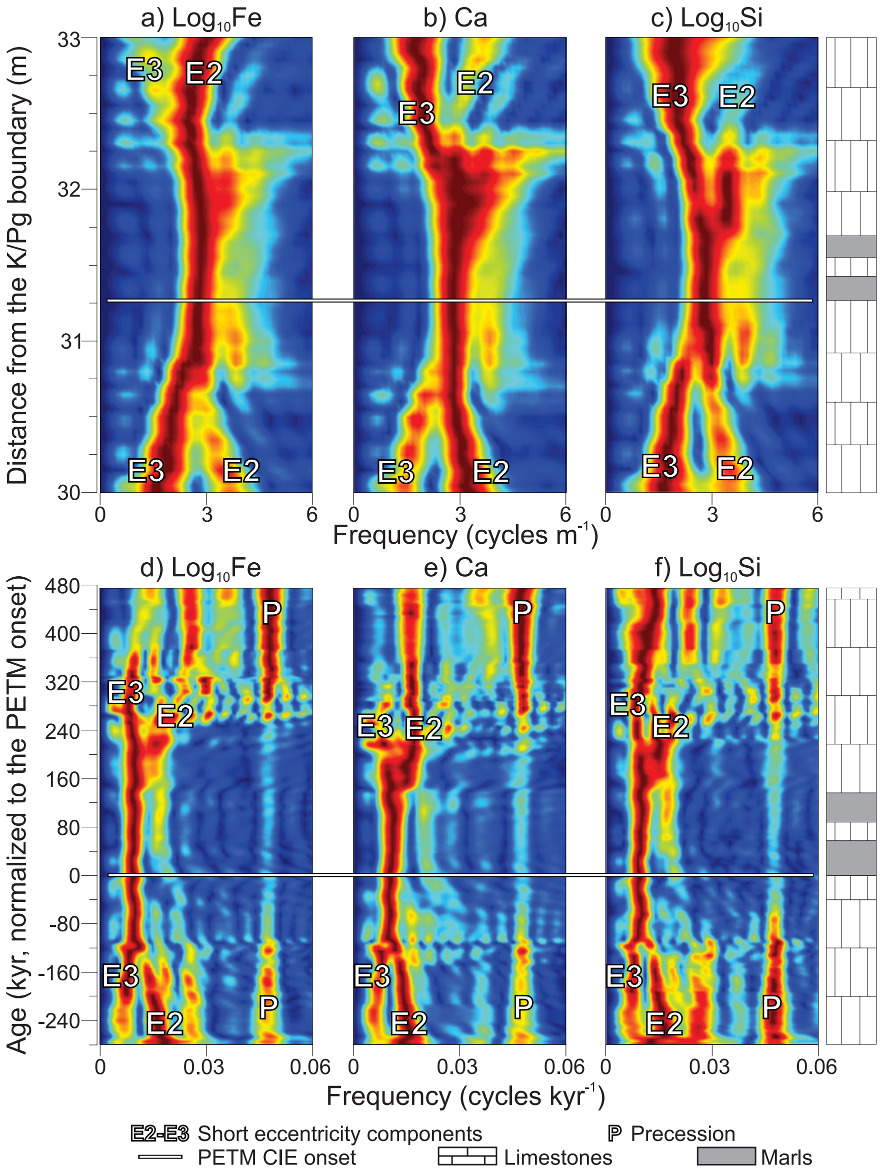
a) $Log_{10}Fe$
b) Ca
c) $Log_{10}Si$
Distance from the K/Pg boundary (m)
33
32
31
30
E3
E2
0
3
6
Frequency (cycles m^{-1})
d) $Log_{10}Fe$
e) Ca
f) $Log_{10}Si$
Age (kyr, normalized to the PETM onset)
480
400
320
240
160
80
0
-80
-160
-240
P
0.03
0.06
Frequency (cycles kyr^{-1})
E2-E3 Short eccentricity components
P Precession
PETM CIE onset
Limestones
Marls

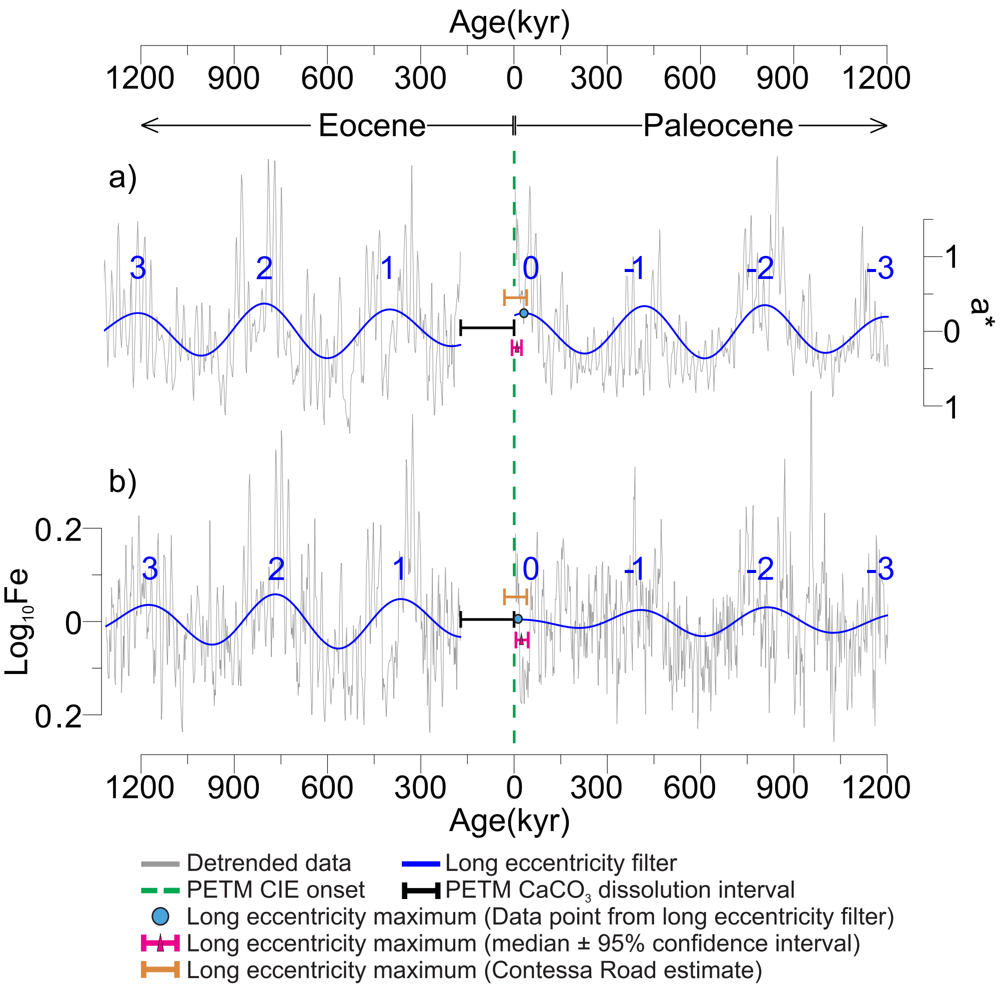
Age(kyr)
1200
900
600
300
0
300
600
900
1200
Eocene
Paleocene
a)
3
2
1
0
-1
-2
-3
1
0
1
a*
b)
0.2
0
0.2
$Log_{10}Fe$
3
2
1
0
-1
-2
-3
1200
900
600
300
0
300
600
900
1200
Age(kyr)
Detrended data
Long eccentricity filter
PETM CIE onset
PETM $CaCO_3$ dissolution interval
Long eccentricity maximum (Data point from long eccentricity filter)
Long eccentricity maximum (median ± 95% confidence interval)
Long eccentricity maximum (Contessa Road estimate)